

Teaching neural networks to generate Fast Sunyaev Zel'dovich Maps

LEANDER THIELE,¹ FRANCISCO VILLAESCUSA-NAVARRO,^{2,3} DAVID N. SPERGEL,^{3,2} DYLAN NELSON,⁴
AND ANNALISA PILLEPICH⁵

¹*Department of Physics, Princeton University, Jadwin Hall, Princeton NJ 08544, USA*

²*Department of Astrophysical Sciences, Princeton University, Peyton Hall, Princeton NJ 08544, USA*

³*Center for Computational Astrophysics, Flatiron Institute, 162 5th Avenue, New York NY 10010, USA*

⁴*Max-Planck-Institut für Astrophysik, Karl-Schwarzschild-Str. 1, 85741 Garching, Germany*

⁵*Max-Planck-Institut für Astronomie, Königstuhl 17, 69117 Heidelberg, Germany*

ABSTRACT

The thermal Sunyaev-Zel'dovich (tSZ) and the kinematic Sunyaev-Zel'dovich (kSZ) effects trace the distribution of electron pressure and momentum in the hot Universe. These observables depend on rich multi-scale physics, thus, simulated maps should ideally be based on calculations that capture baryonic feedback effects such as cooling, star formation, and other complex processes. In this paper, we train deep convolutional neural networks with a U-Net architecture to map from the three-dimensional distribution of dark matter to electron density, momentum and pressure at ~ 100 kpc resolution. These networks are trained on a combination of the TNG300 volume and a set of cluster zoom-in simulations from the IllustrisTNG project. The neural nets are able to reproduce the power spectrum, one-point probability distribution function, bispectrum, and cross-correlation coefficients of the simulations more accurately than the state-of-the-art semi-analytical models. Our approach offers a route to capture the richness of a full cosmological hydrodynamical simulation of galaxy formation with the speed of an analytical calculation.

1. INTRODUCTION

Over the past decade, observations of the cosmic microwave background (CMB) have become one of the most powerful tools for studying the early Universe and for determining its basic properties (age, density, composition). Microwave background observations also have the potential to provide detailed quantitative measurements of the properties of the Universe's recent evolution. Through the thermal Sunyaev-Zel'dovich (tSZ) effect, the microwave observations trace the large-scale distribution of electron pressure; while the kinematic Sunyaev-Zel'dovich (kSZ) effect traces the large-scale distribution of electron momentum (Zeldovich & Sunyaev 1969; Sunyaev & Zeldovich 1970).

High resolution microwave background experiments such as ACT¹, SPT², and upcoming instruments like the Simons Observatory³ and CMB S4⁴, provide ever improving measurements of small-scale fluctuations. Accurate theoretical predictions are essential for extracting the full information from these rich observations. Generating the simulations needed for these accurate predictions is par-

¹ <https://act.princeton.edu>

² <https://pole.uchicago.edu>

³ <https://simonsobservatory.org>

⁴ <https://cmb-s4.org>

ticularly challenging for the SZ effects as they depend not only on the underlying cosmology but also on complex multi-scale processes including feedback from star formation and Active Galactic Nuclei and the rich plasma physics of cluster gas. Hydrodynamical simulations of the Sunyaev-Zel'dovich effects began before the establishment of precision cosmology (Scaramella et al. 1993; da Silva et al. 2000, 2001; Springel et al. 2001). Later works investigated the effects of sub-grid physics (White et al. 2002; Nagai et al. 2007; Pfrommer et al. 2007; Sijacki et al. 2008; Battaglia et al. 2010). Large-scale simulation efforts have enabled direct comparison to microwave observations (Hallman et al. 2007b; Schäfer et al. 2006; Kay et al. 2012; Schaye et al. 2015; Dolag et al. 2016; Spacek et al. 2018; Nelson et al. 2019). Hydrodynamical uniform-resolution simulations are computationally expensive and must adopt a trade-off between large volumes, with robust statistics of high-mass objects, and high numerical resolution to better capture the important physical processes.

Cosmologists have been taking a variety of approaches to more efficiently generate predicted tSZ maps. Most work builds on numerical simulations. Early papers assumed that on large scales the gas pressure traces the dark matter distribution (Persi et al. 1995; Refregier et al. 2000). In order to more accurately describe the non-linear evolution, halo model approaches have been developed, starting from Komatsu & Kitayama (1999) and Komatsu & Seljak (2002). These assume that the halos have a characteristic profile (Komatsu & Seljak 2001), depending on mass and redshift and possibly a few other parameters. A variety of other analytical approaches in the halo model framework have been developed (Lee & Suto 2003; Ostriker et al. 2005; Hallman et al. 2007a; Bode et al. 2007, 2009; Shaw et al. 2010; Efstathiou & Migliaccio 2012; Capelo et al. 2012; Shi & Komatsu 2014). These have some free parameters that are calibrated off observations of low-redshift objects. A comparison of different analytical halo model approaches is performed in Trac et al. (2011). Recent work has calibrated these halo electron pressure profiles off of numerical simulations (Allison et al. 2011; Battaglia et al. 2012; Nelson et al. 2014; Le Brun et al. 2017; Gupta et al. 2017; Planelles et al. 2017; Mead et al. 2020), or observations (Afshordi et al. 2007; Atrio-Barandela et al. 2008; Arnaud et al. 2010; Chaudhuri & Majumdar 2011; Planck Collaboration et al. 2013; Zandanel et al. 2014; Le Brun et al. 2014; Ramos-Ceja et al. 2015). A common theme of these semi-analytical models is the assumption of symmetries (often spherical) and the restriction to a small set of variables describing a given halo. Especially the neglect of halo sub-structure leads to errors in summary statistics (Battaglia et al. 2012).

Treatments of the kSZ effect begin with linear theory (Ostriker & Vishniac 1986; Vishniac 1987; Jaffe & Kamionkowski 1998), and then were extended to non-linear scales (Valageas et al. 2001; Ma & Fry 2002; Zhang et al. 2004; Park et al. 2016). More recent works use numerical simulations to calibrate the analytic treatment (Shaw et al. 2012; Alvarez 2016; Park et al. 2018).

In this work we use a different approach, schematically illustrated in Fig. 1. We employ deep learning techniques to find the mapping between the spatial distribution of dark matter⁵ from gravity-only cosmological simulations and (1) electron pressure, (2) electron density, and (3) electron momentum from the corresponding state-of-the-art full-physics hydrodynamical realizations. In particular, we use simulations from the IllustrisTNG project (Springel et al. 2018; Naiman et al. 2018; Nelson et al. 2018; Marinacci et al. 2018; Pillepich et al. 2018a; Nelson et al. 2019). The advantage of this method with respect to the semi-analytical models is that gravity-only simulations are accurate enough to model the clustering of matter and halos down to rather small scales, and deep learning can trans-

⁵ For brevity, here and in the remainder of this paper we use the phrase “dark matter” to mean the matter field obtained in a gravity-only simulation.

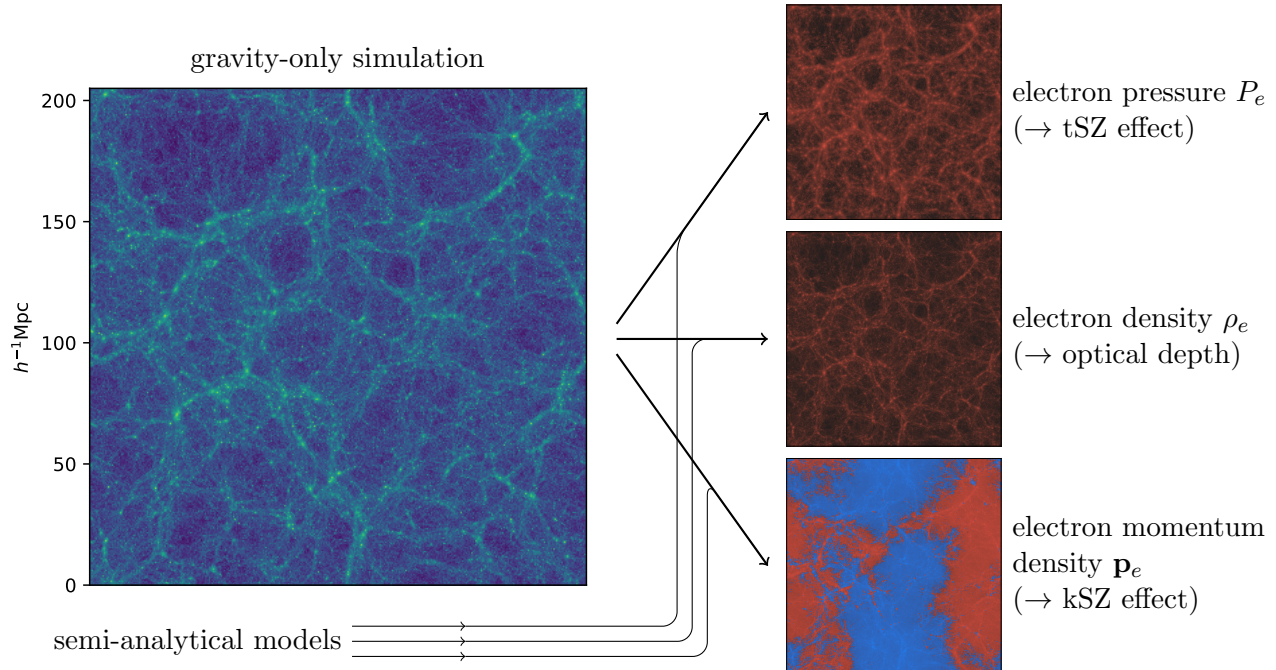


Figure 1. Schematic illustration of the approach taken in this work. We use properties of the matter field from gravity-only cosmological simulations, on the left, as input into convolutional neural networks which predict the electron gas properties via training based on the corresponding full-physics hydrodynamical realization, on the right. The networks utilize simulation-calibrated semi-analytical models for the targets, so that only residuals with respect to the hydrodynamical simulation output are required to be learned.

form their output to account for baryonic effects, capturing non-gravitational processes while avoiding oversimplifications such as spherical symmetry.

Machine learning has previously been used for similar tasks, for example to generate two-dimensional maps of the tSZ effect (Tröster et al. 2019), and populating gravity-only simulations with galaxies (Xu et al. 2013; Zhang et al. 2019; Agarwal et al. 2018; Jo & Kim 2019; Moster et al. 2020).

We approach this work as part of a broader program consisting of predicting baryonic observables from gravity-only simulations, or even directly from the initial conditions (He et al. 2019). One application of particular interest would be the prediction of cross-correlation statistics between different observables. Because of our focus on cross-correlations, we are primarily interested in generating the low-redshift kSZ signal and defer the discussion of the high redshift signal to future work. Our current approach assumes that there is an injective map between the matter field and the observables of interest; we discuss stochasticity (which is not captured in our approach) in Section 6.

This approach will allow us to quickly generate tSZ and kSZ maps, over large areas of the sky, with the astrophysical model of the IllustrisTNG simulation (Weinberger et al. 2017; Pillepich et al. 2018b), but in comparatively negligible time (see the figures quoted in Section 6). Those maps can be used to extract cosmological and astrophysical information from CMB observations alone, but also allow the modeling of cross-correlations such as tSZ-weak lensing or kSZ with spectroscopic surveys.

This paper is organized as follows. We describe the physics of the tSZ and kSZ effects in Section 2. Section 3 outlines the methods used in the analysis. Section 4 describes the challenge introduced by sparsity: rare massive clusters contribute a significant fraction of the tSZ signal and dominate the higher moment statistics of the maps. The section describes the use of zoom-in simulations of high density regions to augment the data set and ameliorate this issue. We show the results of our work in Section 5. Finally, in Section 6 we draw the conclusions. Some technical details are collected in the Appendices.

2. PHYSICAL BACKGROUND

At low frequencies, clusters cast shadows against the microwave sky: in the 90 and 150 GHz Planck, ACT and SPT maps, the tSZ effect makes clusters appear as cold spots. This effect arises from random motions of thermal electrons which scatter CMB photons into higher energy states. It produces a non-blackbody distortion in the primary CMB's Planckian spectrum, yielding a brightness temperature decrement (increment) at low (high) observation frequencies ν . It is usually parameterized in terms of the dimensionless Compton- y parameter, given by

$$y = \sigma_T \int_{\text{LOS}} dr \frac{P_e}{m_e}, \quad (1)$$

where $\sigma_T = (8\pi e^4/3)m_e^{-2}$ is the Thompson cross-section for electron-photon scattering, r is physical distance along the line of sight (LOS), $P_e = n_e T_e$ is electron pressure, and m_e is the electron mass. The dependence on the choice of line of sight \mathbf{n} has been suppressed. Thus, the tSZ effect is a measure of the line-of-sight integrated thermal energy density in electrons.

The kinematic SZ (kSZ) effect, on the other hand, is sourced by coherent motion of the electrons. To leading order it preserves the blackbody energy distribution, yielding a shift in the local CMB temperature. We can write down a parameterization similar to the tSZ Compton- y , referred to as the Doppler- b parameter:

$$\mathbf{b} = \sigma_T \int_{\text{LOS}} dr \frac{\mathbf{p}_e}{m_e} e^{-\tau(r)}, \quad (2)$$

where

$$\tau(r) = \sigma_T \int_0^r dr' \frac{\rho_e}{m_e} \quad (3)$$

is the optical depth (average number of Compton scattering events up to r) and \mathbf{p}_e is the electron momentum density (momentum per unit volume).

For reference, the dimensionless parameters introduced above are related to the observed shifts in the CMB temperature by

$$\frac{\Delta T_{\text{tSZ}}(\mathbf{n}, \nu)}{T_{\text{CMB}}} = y(x \coth x/2 - 4), \quad x \equiv \nu/T_{\text{CMB}}; \quad (4)$$

$$\frac{\Delta T_{\text{kSZ}}(\mathbf{n})}{T_{\text{CMB}}} = -\mathbf{b} \cdot \mathbf{n}. \quad (5)$$

In the late-time universe, both SZ effects are predominantly sourced by electrons bound to dark matter halos. The tSZ effect is mostly sourced by the hot electron gas in the cluster center (due to the dependence on electron temperature), and the cluster integrated signal scales roughly as $Y \propto M_{\text{halo}}^{5/3}$

(Sunyaev & Zeldovich 1970). In contrast, the kSZ effect does not receive this temperature bias and is thus more sensitive to the cool electron gas in cluster outskirts, lower mass halos, and the IGM.

As we explain in Section 3.1, our procedure begins with semi-analytical models for the desired electron gas properties. For the electron pressure, we make use of the simulation-calibrated model from Battaglia et al. (2012), hereafter B12, which gives a simple fitting function for the electron pressure as a function of halo mass and redshift:

$$P_e^{\text{model}}(\mathbf{x}) = \sum_{\text{halos } h} \text{B12}(M_h, |\mathbf{x} - \mathbf{x}_h|). \quad (6)$$

The B12 semi-analytical model is calibrated on a particular cosmology with given assumptions on sub-grid baryonic effects.

In contrast to the electron pressure, we do not use a halo model fitting function (Battaglia 2016) for the electron density, as we find that a simple linear fit relating dark matter and electron density with an additional Gaussian smoothing is good enough for the purposes of this work:

$$\rho_e^{\text{model}}(\mathbf{x}) = A \times [\text{Gaussian}(\sigma = 80 h^{-1} \text{kpc}) \otimes \rho_m](\mathbf{x}), \quad (7)$$

with A a scalar that was fitted to the TNG300 simulation. The convolution kernel was chosen by visually inspecting some halos, its precise shape and width are of little importance.

From this, we finally construct our semi-analytical model for the electron momentum density:

$$\mathbf{p}_e^{\text{model}}(\mathbf{x}) = \rho_e^{\text{model}}(\mathbf{x}) \mathbf{v}_m(\mathbf{x}), \quad (8)$$

where \mathbf{v}_m is the dark matter velocity field. In particular, we do not include any velocity bias between dark matter and baryon velocities.

3. METHODS

In this section, we describe the methods used to prepare the data, as well as the general set-up for the machine learning procedure (input and target data, network architecture). We defer the solutions we developed for specific challenges arising from the properties of the data to the next section.

3.1. Data preparation

For the majority of this work, we use the TNG300-1 (hydrodynamical) and TNG300-1_DM (gravity-only) $z = 0$ snapshots (Springel et al. 2018; Naiman et al. 2018; Nelson et al. 2018; Marinacci et al. 2018; Pillepich et al. 2018a; Nelson et al. 2019). We also make use of additional zoom-in hydrodynamical simulations, as discussed in Section 4.1; using an available subset of halos from the TNG-Cluster sample (Nelson et al. in prep.). Details on the pixelization of the various fields are given in Appendix A.

In addition to the dark matter properties, we also use simple semi-analytical models for the output as input data. The reason for this is that neural networks train faster on residuals than on the entire target. We defer the reader to the previous section for a description of how these semi-analytical models have been constructed for the different targets.

3.2. Sampling

We expect the mapping between the dark matter field and the target properties of the electron gas to be dominated by operators whose spatial support does not exceed length-scales of a few Mpc. Therefore, we choose our training samples as local boxes, as described in more detail in Appendix B.

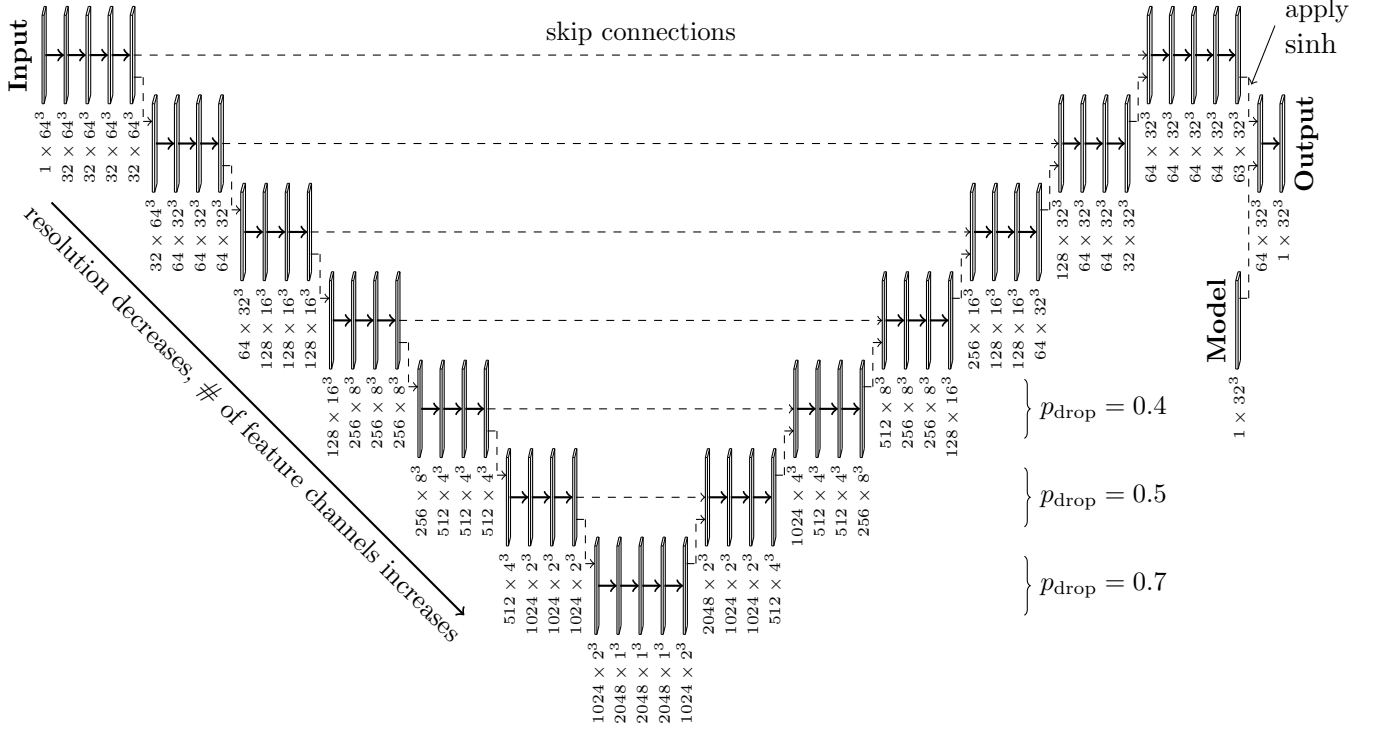


Figure 2. U-Net architecture for the CNN used in predicting electron pressure and density from dark matter distributions in 3D. The layer dimensions are given in the format ($\#$ of feature channels) \times grid size. The dashed lines represent copies, while the solid arrows are convolutional operations with 3^3 -sized filters (except for the very last operation, where the channels are simply collapsed into the output). If more than one dashed line ends at a single layer we concatenate along the feature channel direction. In the lowest three levels we apply dropout of entire feature channels with the probabilities given. We usually apply batch normalization, except wherever dropout is used. All activation functions are ReLUs. The network used to predict the electron momentum density is of similar structure, with the following differences: the semi-analytical model is not concatenated but rather multiplied with the first channel of the network representation; no sinh function is applied; since the resolution is a factor 2 smaller the network is smaller; in the two levels with highest resolution we apply **Hardshrink** activation functions. Most of these modifications are natural consequences of the negative-positive symmetry of the momentum data.

3.3. Neural network

Having defined the input and target data, we now discuss the neural network architecture. Given the locality of the problem as well as translational, rotational, and parity invariance, a deep convolutional neural network architecture is the logical choice. Motivated by previous successes in similar applications (e.g., He et al. 2019; Zhang et al. 2019), we choose a U-Net architecture, displayed in Fig. 2 (this network was used for electron pressure and density as target data, the architecture for the electron momentum density was slightly modified to take the sign symmetry of the data as well as lower resolution into account). The general idea of the U-Net is that while the receptive field increases in deeper layers, the number of feature channels increases. This allows the network to find more spatial correlations on larger scales. Skip connections (horizontal dashed lines in the figure) make it easier for the network to retain more local, high resolution features. Note that the semi-

analytical model is fed into the network at a rather late stage, this makes it easier for the network to recognize that the target is close to the semi-analytical model with small residuals that need to be learned in the deeper layers. More details on the network architecture may be found in the caption of Fig. 2.

3.4. Training procedure

To train the network, we use the Adam optimizer with $\vec{\beta} = \{0.9, 0.999\}$ and choose samples from the training set according to a strongly biased selection function, as described in Section 4.1. These samples consist of in- and output boxes which are described in Appendix B (there, we also specify the splitting into training, validation, and testing data). Although there is no natural definition of an epoch, for convenience, we define an epoch as 8192 training samples. The validation loss is evaluated on a random subset (chosen according to the same selection function as for the training set) of 256 boxes from the validation set. We find that a batch size of 32 yields the best performance. We generally start training with a learning rate of 10^{-3} , train for about 100 epochs, and then resume training from the state of the network with the best validation loss. We adjust the learning rate whenever we see the validation loss to become dominated by noise over any perceptible downwards trend. While during training only the loss function discussed in Section 4.1 is computed, after each training run (i.e. every ~ 100 epochs), we evaluate the network on the whole validation box and compute power spectrum, cross-correlation coefficient with the reference hydrodynamical simulation, and one-point PDF. We base our decisions regarding the tuning of hyperparameters, changes in network architecture, and the eventual stop of training principally on these summary statistics as well as the validation loss curve.

We perform the usual data augmentation of rotations, reflections, and transpositions; in addition, in order to avoid overfitting, we multiply input data and target by voxel-wise Gaussian noise of 10% standard deviation and unit mean. Although it is impossible to explore all directions in the space of hyperparameters, we are confident that with about 200 runs with different hyperparameters and network architectures we have found a relatively well optimized training procedure and network architecture.

4. CHALLENGE: SPARSITY

The main challenge we need to overcome to train the neural network can be summarized as the sparsity of the dataset. In this section, we will argue that this problem comes in two different, but related, aspects, and explain the strategies we use to solve it. We will concentrate on the case of electron pressure here, the arguments carry over to electron density and electron momentum density.

4.1. Few interesting voxels

The first aspect to consider is the fact that only very few voxels are actually “interesting”, in the sense that they contribute to any commonly used summary statistics. This point is illustrated in Fig. 3, where we plot the electron pressure power spectrum. While the solid blue line is the power spectrum for the target TNG300 hydrodynamical box, the dashed lines result from setting voxels with electron pressure below varying thresholds to zero. We observe that only voxels with $P_e \gtrsim 10^{-2}\sigma(P_e)$ are relevant (this argument is only rigorous for the case of the power spectrum, but it is clear that for higher order statistics the situation is even more severe). Referring now to the solid lines in Fig. 4, in which we plot the probability distribution function (PDF) and cumulative distribution function

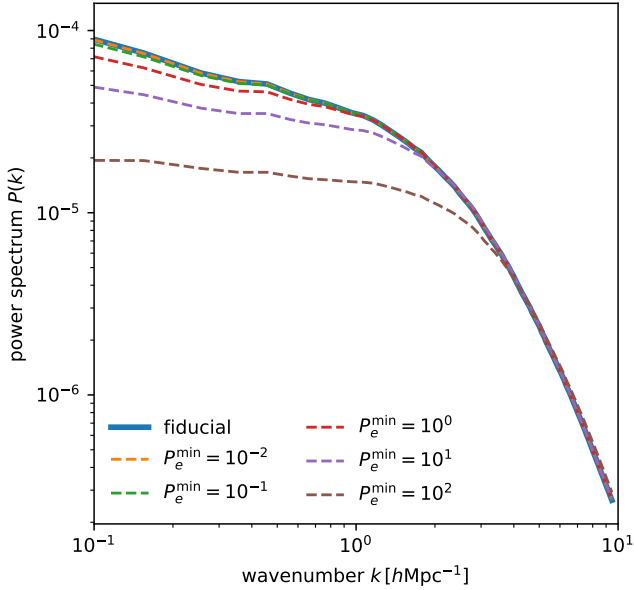


Figure 3. *solid blue:* electron pressure power spectrum for 20% of the TNG300 box. *dashed:* the same with electron pressure values below minimum values P_e^{\min} (given in units of $\sigma(P_e)$) set to zero. It can be seen that the electron pressure power spectrum can be reproduced using only voxels with $P_e \gtrsim 10^{-2}\sigma(P_e)$. These voxels represent only a small fraction of the entire box, as illustrated in Fig. 4.

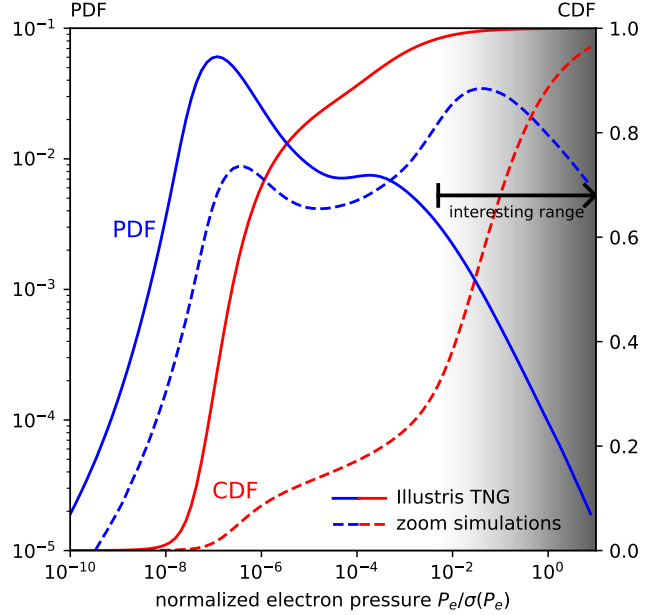


Figure 4. Illustration of the sparsity problem in the electron pressure distribution. Plotted are both probability distribution function (PDF; blue) and cumulative distribution function (CDF; red) for the TNG300 volume (solid) and the 181 TNG-Cluster zoom-in simulation boxes (dashed). The shaded area labeled “interesting range” was chosen according to the conclusions from Fig. 3. In the reference uniform-volume simulation, TNG300, only of order 1 % of the voxels fall into the “interesting” range.

(CDF) of the electron pressure, we observe that those relevant voxels constitute only a tiny fraction (of order 1 %) of the simulation volume.

The small fraction of interesting voxels implies that a naive training procedure in which we would randomly pick training samples from the simulation volume would be highly inefficient. Thus, we solve this first aspect of the sparsity problem by biasing the training samples. We know that the high electron pressure voxels are found in massive halos. Therefore, it seems natural to bias the sample selection such that always at least one halo of a given minimum mass is to be found in any training sample.

In the case of the electron density as target, we find that biasing according to the selection function⁶

$$w_{\rho_e}(M_{500c}) \propto \Theta(M_{500c} - 10^3)(\log_{10} M_{500c})^{0.25} \quad (9)$$

with Θ the Heaviside function gives good results.

⁶ From here onwards, wherever not otherwise stated, we use the following units: unit mass = $10^{10} h^{-1} M_{\odot}$; unit length = $1 h^{-1} \text{kpc}$; unit speed = 1 km/s .

Note that the actual halo mass function of the training samples is *not* identical to Eq. (9) but rather equals $w(M)$ times the TNG300 mass function (since $w(M)$ chooses from the available halos).⁷

In the case of the electron momentum density, we find that a less aggressive selection function works best:

$$w_{\mathbf{p}_e}(M_{500c}) \propto \Theta(M_{500c} - 10^3). \quad (10)$$

In the case of electron pressure, the biasing schemes described above are not sufficient. The reason is that the integrated electron pressure in halos of mass M_{halo} is not simply $\propto M_{\text{halo}}$, but scales as $\propto M_{\text{halo}}^{5/3}$. To overcome this problem, for electron pressure alone, we do not use the original TNG300 simulation for training samples, but instead draw our training samples from additional zoom-in simulations centered on massive halos. These are performed with the same astrophysical galaxy-formation model as TNG300 and at similar resolution, but focus on high-mass halos (Nelson et al. in prep.). Hence, these zoom-in simulations have a very different halo mass function compared to the TNG300 volume; in particular, while the TNG300 simulation only has a few halos with $M_{200c} > 10^{14.5} h^{-1} M_{\odot}$, the majority of the zoom-in primary objects are more massive than this. The electron pressure PDF and CDF obtained in these highly biased training samples are plotted as the dashed lines in Fig. 4. It can be seen that about 70% of the voxels from the TNG-Cluster training set fall in the “interesting” range, according to the conclusions derived from Fig. 3. We point out that for the zoom-in simulations we did not have gravity-only simulations available. This implies that the mapping from input (which is gravity-only during validation and testing) to output is not exactly identical for the TNG-Cluster training samples and the TNG300 validation and testing set. We would expect this effect to be most prominent on small scales.

4.2. Tailed distributions

The second aspect of the sparsity problem is the remaining high dynamic range of the voxel values. Even though we have argued that the network can essentially ignore any $P_e < 10^{-2}\sigma(P_e)$, the remaining “interesting” electron pressure values still span several orders of magnitude (c.f. Fig. 4). Likewise, the dark matter density which we take as the network input also has a tailed distribution.

The solution for the problem of the tailed distribution of input data is relatively standard (e.g., Tröster et al. 2019), and consists in shrinking the dynamic range of the input data (this can be interpreted as a generalization of the unit-variance zero-centred rescaling that is standard practice in many machine learning applications). We use the transformation

$$\tilde{x}_{\text{DM}} = a[\log(1 + bx_{\text{DM}}) - c], \quad (11)$$

where b is related to the standard deviation of the field, and a and c are obtained by requiring zero mean and unit variance. For reproducibility, we list the values of these parameters in Appendix C.

The tailed target distribution constitutes a challenge in two ways. First, vanilla neural networks are not designed for the flow of high-dynamic-range data; standard architectures and training procedures are calibrated for well behaved distributions of the internal representation. To address this problem, we take two steps: (1) as mentioned before, we provide a semi-analytical model for the target, so

⁷ To be precise: we make a list of TNG300 halos with masses above the argument in the Θ -function, assign weights to them according to $w(M)$ and then, in each training step, randomly choose a halo according to these weights. The input (gravity-only) sample box, whose geometry is described in Appendix B, is then chosen such that the halo’s center falls into one of its voxels, with equal probability for each voxel to contain the halo center.

that the network only has to learn the difference between target and semi-analytical model⁸; (2) before concatenating the network output with the semi-analytical model, we apply the sinh function to the network output, as illustrated in Fig. 2. We empirically found a sinh to work better than the exponential function, presumably the network prefers the possibility that some of the output data fall into the approximately linear range of the sinh. Both measures serve to decrease the dynamic range of the internal representation⁹.

The second challenge stemming from the tailed target distribution is related to the choice of loss function. It is clear that for good performance on summary statistics such as the power spectrum we would like to use a loss function of the form $L(p, t) = \Sigma(p - t)^2$, where p and t are the prediction and target respectively, and Σ schematically indicates summation over voxels. However, empirically it is found that starting training with this loss function leads to unstable behaviour, presumably because large gradients are backpropagated due to the high dynamic range of t .

Thus, in order to stabilize training, we adopt a time-dependent loss function,

$$L_\tau(p, t) = \sum [f_\tau(p) - f_\tau(t)]^2; \quad (12)$$

$$f_\tau(x) = e^{-\tau/\tau_0} \text{sgn}(x) \log(1 + 10|x|) + (1 - e^{-\tau/\tau_0})x, \quad (13)$$

where p and t have been divided by the standard deviation of the target field. The parameter τ measures time in units of epochs, and we found that a good choice for τ_0 is about 30-100, with lower values leading to more unstable training, while larger values prolong the training process unnecessarily and increase the risk of overfitting. The transformation f_τ smoothly interpolates between the more gentle $\log(1 + x)$ and a linear function, converging at the desired mean squared error (MSE) loss as training progresses beyond τ_0 epochs. The signum function and absolute value are only required for the electron momentum density which can have positive and negative values. We always evaluate the validation loss with $\lim_{\tau \rightarrow \infty} L_\tau$, i.e. the traditional MSE, since it is a good measure to quantify performance on the power spectrum and other commonly used summary statistics.

5. RESULTS

Having explained the methods, we now proceed to present our results; we will split this section into four parts: In Section 5.1, we present the results for the electron pressure (i.e. tSZ effect) as target, Section. 5.2 and 5.3 are concerned with the electron density and momentum density respectively, and in Section 5.4 we consider cross-correlations between different fields. We will give somewhat more detail on the electron pressure, with the results generalizing to a large extent to the other two cases. As usual in machine learning, the results here are evaluated on a testing set, i.e. parts of the simulation the network has not seen before, as described at the end of Appendix B. We will compare the performance of the network with that of the simple semi-analytical models we use as a guess for the target. It should be emphasized that these semi-analytical models are not necessarily the best we could possibly construct; however, they should serve as useful reference points.

⁸ As can be seen from the network architecture, Fig. 2, the network has the freedom to rescale the semi-analytical model by a constant factor. In principle it could set this constant to zero if it deems the semi-analytical model too inaccurate, but empirically we find it to be close to unity. Thus, the word ‘‘residual’’ is to be understood in a somewhat generalized sense.

⁹ In fact, we examined the values of weights and biases after training and found them to be approximately Gaussian distributed around mean zero with variance of order unity, which confirms the effect we expect the mentioned techniques to have.

5.1. Electron pressure

The network was trained with electron pressure as target on the mentioned zoom-in simulations. The training set is relatively small (181 independent simulation boxes with enhanced resolution centered around massive halos). We observe the disadvantage of such a small training set in that the network starts overfitting after 176 epochs, when we halt training. Mixing samples from the TNG300 volume with the zoom-in simulations to enlarge the training set does not seem to yield improved performance in our experiments, indicating that the network updates are driven by the high-density regions in the extremely massive clusters.

In Fig. 5, we plot the electron pressure power spectrum; here, and elsewhere, computed using `nbodykit`¹⁰ (Hand et al. 2018). We plot two versions of the B12 semi-analytical model, the lower curve being the original output and the upper curve having the electron pressure values rescaled by a constant factor to make for a fairer comparison. In terms of the power spectrum, the network's prediction matches the TNG300 target result better than the B12 semi-analytical model on all scales and shows very good agreement with the target on small scales ($k \gtrsim 1 \text{ hMpc}^{-1}$). It should be emphasized, however, that B12 was calibrated on a different simulation.

The deficit in power on larger scales ($k \lesssim 1 \text{ hMpc}^{-1}$) is consistent with the zero-order approximation that the network neglects to predict electron pressures below a certain threshold (c.f. Fig. 3). We point out that if this explanation is correct, the lack of power is not particularly worrisome since upon projection along the line of sight (to obtain the Compton- y observable Eq. 1) the low pressure values will be further diminished in their contribution to any relevant summary statistics. In order to test this interpretation, we project the electron pressure along one cartesian axis and compute the power spectrum of the resulting two-dimensional field; this is plotted in Fig. 6. We observe that upon projection the agreement between the network prediction and the target improves, consistent with our explanation for the lack of power. It is quite conceivable that if one were to construct a complete tSZ map, i.e. project up to redshift 1100, the discrepancy would entirely disappear.

While the power spectrum measures the amplitudes of the different modes, the cross-correlation coefficient between two fields A and B

$$r_{AB}(k) \equiv \frac{P_{AB}(k)}{\sqrt{P_{AA}(k)P_{BB}(k)}} \quad (14)$$

is a measure of the correlation between their phases. We plot the correlation coefficient with respect to the target electron pressure in Fig. 7 (a perfect prediction would have unit cross-correlation with the target field). Again, the network matches the reference simulation better than the semi-analytical model and maintains a correlation of 98% up to $k < 2 \text{ hMpc}^{-1}$.

While power spectrum and correlation coefficient are useful summary statistics, non-Gaussian statistics are of great importance for non-linear fields such as the tSZ. In Fig. 8, we plot the one-point PDF; again we observe very good agreement between the network prediction and the target, while the semi-analytical model appears to lack high-pressure voxels. This is a strong indication that the simulation details (in particular the amount of feedback) are sufficiently different between the IllustrisTNG simulations and the simulations the B12 semi-analytical model has been calibrated on that a direct comparison between the two is not particularly meaningful. Note that on linear P_e -scale

¹⁰ <https://github.com/bccp/nbodykit>

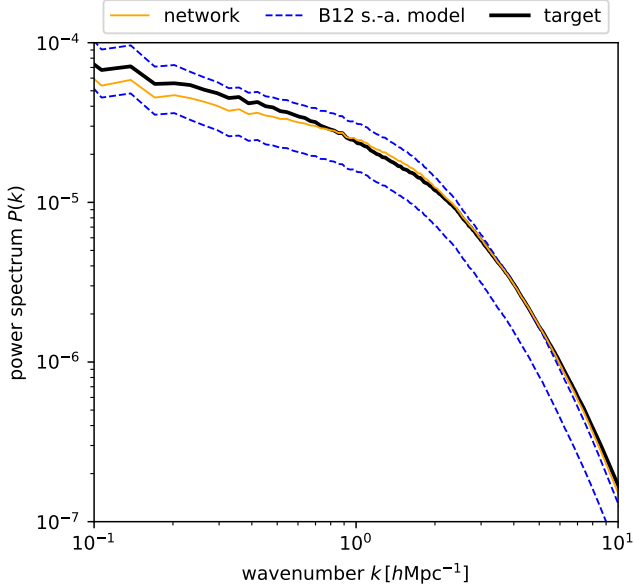


Figure 5. Electron pressure power spectrum. We plot two versions of the B12 semi-analytical model: the lower curve is the original output, the upper curve is the same rescaled by a constant factor to make the comparison fairer. While we observe excellent agreement between network prediction and target result (from the TNG300 hydrodynamical simulation), there is a lack of power ($\sim 20\%$) on large scales. This is likely related to errors in the prediction of low-pressure voxels, as demonstrated in Fig. 6.

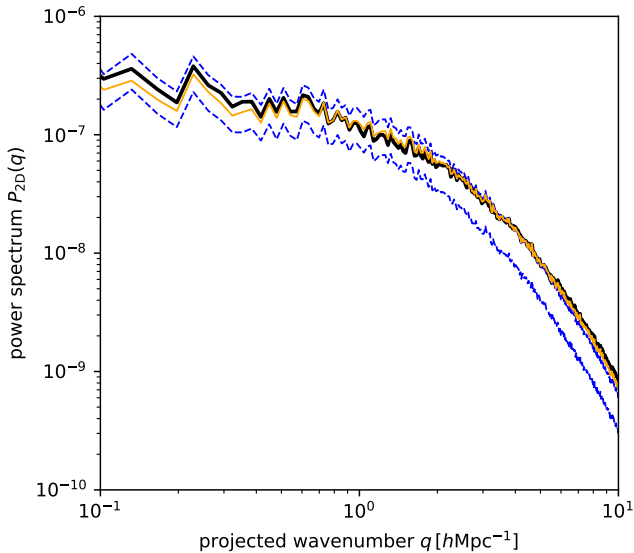


Figure 6. Electron pressure projected power spectrum, illustrating that upon projection along one axis the small electron pressure values, which the network is unable to recover correctly, are of lesser importance, compared to the 3-dimensional power spectrum in Fig. 5.

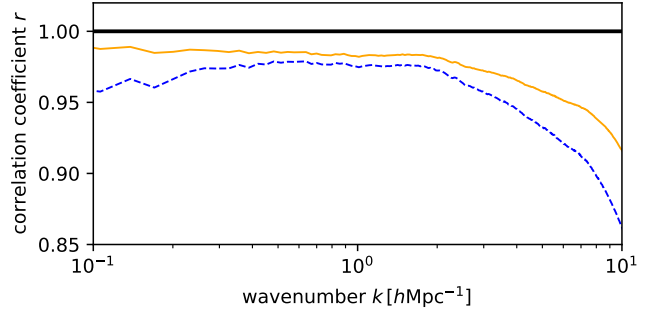


Figure 7. Electron pressure cross-correlation coefficient between network prediction/B12 semi-analytical model output and the target simulation field. Note that this measure is unaffected by the rescaling of the B12 semi-analytical model employed in Fig. 5.

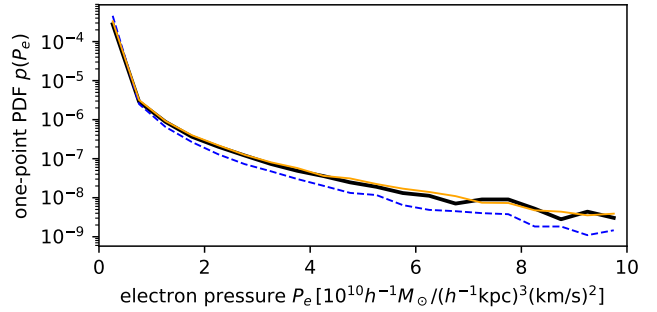


Figure 8. Electron pressure one-point PDF. The network prediction matches the target simulation very well. We only plot the original B12 semi-analytical model, not the rescaled version shown in Fig. 5.

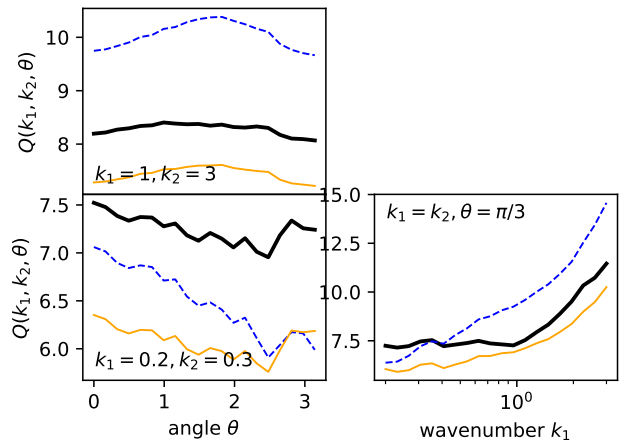


Figure 9. Some (reduced) bispectra for the electron pressure. Wavenumbers are given in units of $h\text{Mpc}^{-1}$. *Upper left*: small scales with varying triangle shapes, *lower left*: large scales with varying triangle shapes, *lower right*: varying scales with fixed equilateral triangle shape.

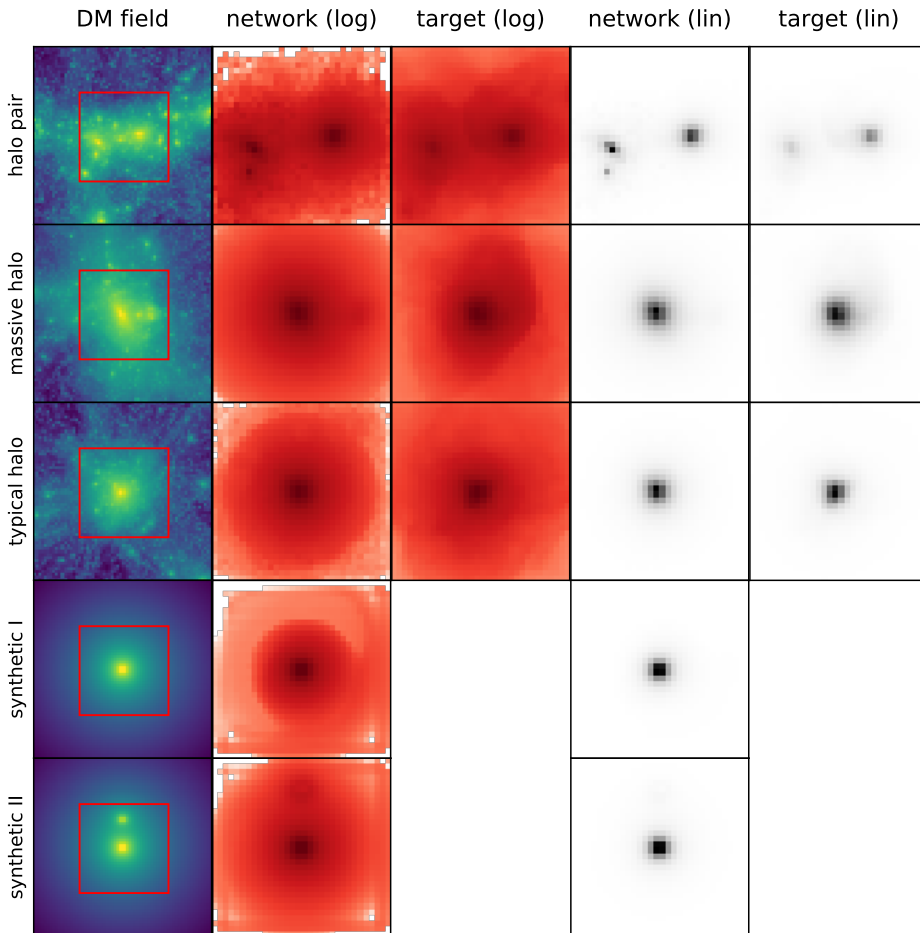


Figure 10. Some individual halos. We plot the matter density and electron pressure (both network prediction and simulation target), projected across 6.4 and $3.2 h^{-1}\text{Mpc}$ respectively. For the electron pressure, both logarithmic and linear scales are provided. The red boxes in the left column indicate the extent of the target boxes in the dark matter boxes (c.f. the discussion of padding in Appendix B). The first three rows are taken from the TNG300 box, while the last two are synthetic pure NFW dark matter halos for which we do not have a hydrodynamical simulation target available. Note that the color scales are different in each row in order to make interpretation easier.

the discrepancies at low values, which explain large-scale differences in the power spectrum, are not visible.

Another non-Gaussian statistic is the bispectrum, which we plot in Fig. 9 for several different triangle configurations; the computation was performed using `Pylians`¹¹ (Villaescusa-Navarro 2018). The network shows agreement with the target at the 20% level. It should be pointed out that we did not use the bispectrum during cross-validation; one could imagine a training procedure where it is taken into consideration as well if more accurate predictions are needed. Another alternative would be to use a more general loss function if bispectrum predictions are desired. The large-scale bispectrum (lower left corner of Fig. 9) is the only summary statistics in this section for which the B12 semi-analytical model matches the simulation better than the network’s prediction.

In order to gain more intuition, we present images of the electron pressure in several different halos in Fig. 10. The first three rows are taken from the TNG300 box; for the ones labeled “massive halo” and “typical halo” (with total halo masses of $M_{200c} = 8.8 \times 10^{14}$ and $2.6 \times 10^{14} h^{-1} M_{\odot}$, respectively); we observe very good agreement between network prediction and target. On the other hand, the

¹¹ <https://github.com/franciscovillaescusa/Pylians>

network predicts too high electron pressure values for the “halo pair”, possibly it is unable to take the long-range interaction between the two halos into account, the number of such situations in the training set being very small. The last two rows are synthetic pure NFW dark matter profiles. For these we choose a halo mass of the primary object as $M_{200c} = 10^{14} h^{-1} M_{\odot}$; the last row also contains a smaller halo with $2 \times 10^{13} h^{-1} M_{\odot}$. Given these masses (and redshift $z = 0$), we use the concentration-mass relation from [Duffy et al. \(2008\)](#) and the density profile from [Navarro et al. \(1997\)](#) to create the “synthetic” input data. We observe that the network has learned spherical symmetry quite well (the small deviations near the edges of the box are completely irrelevant for the loss function, as evidenced by the plots in linear color scale).

The network performance for electron pressure is remarkable given that it was trained on the TNG-Cluster sample, which is unusually small (for U-Net standards) and highly biased, and which furthermore is expected to show some small-scale differences to the test set of TNG300 halos. We expect these small-scale differences because we do not have gravity-only zoom-in simulations available, so that the input data will be slightly different due to feedback and baryon-baryon interactions. The fact that these small-scale differences seem to be of minor importance indicates that the network does not assign much importance to features at the voxel scale; this fact gives us confidence in generalizability. The good performance despite strong biasing of the training set is interesting as well: we have mentioned that most of the halos in the training set are more massive than the most massive halos in the testing set. We interpret the fact that our procedure still works as an indication that the mapping between dark matter and electron gas may be dominated by sub-halo-scale features.

5.2. Electron density

As mentioned in Section 4.1, learning the mapping from matter to electron density does not require such a strongly biased selection of the training samples as it did for the electron pressure. Thus, we can use sub-volumes of the TNG300 box as training samples, giving us a substantially larger training set. In this case, we do not observe any problems with overfitting. Since we expect the network to utilize quite similar features in its prediction of both electron pressure and density, we use the same network architecture and start the training for electron density with the best trained version for the electron pressure. Confirming our expectation, the network quickly (within about 20 epochs) adapts to the new target and converges slowly afterwards. Since no overfitting occurs, we train up to 210 epochs, when the validation loss shows no significant improvement anymore.

In Fig. 11, we plot the electron density power spectrum, which shows remarkable agreement between network prediction and target. Similarly, the cross-correlation coefficient with the target simulation, plotted in Fig. 12, exceeds 98% up to $k < 4 h\text{Mpc}^{-1}$. Finally, the one-point PDF, plotted in Fig. 13, also shows good agreement. The relatively noisy behaviour in the high-density tail (compared to Fig. 8) occurs because the volume of the testing box is only 10% of the volume in the electron pressure testing set.

In summary, the electron density is an easier target compared to the electron pressure. Due to the better behaved distribution of target values, we are able to use a much larger training set¹², preventing any problems with overfitting and leading to very good performance on the testing set. The fact that, apart from the change in training set, no modification to the network architecture

¹² While we have 181 primary objects in the TNG-Cluster zoom-in simulations available, there are 1416 halos in the TNG300 with masses larger than the cut-offs in Eqs. (9), (10).

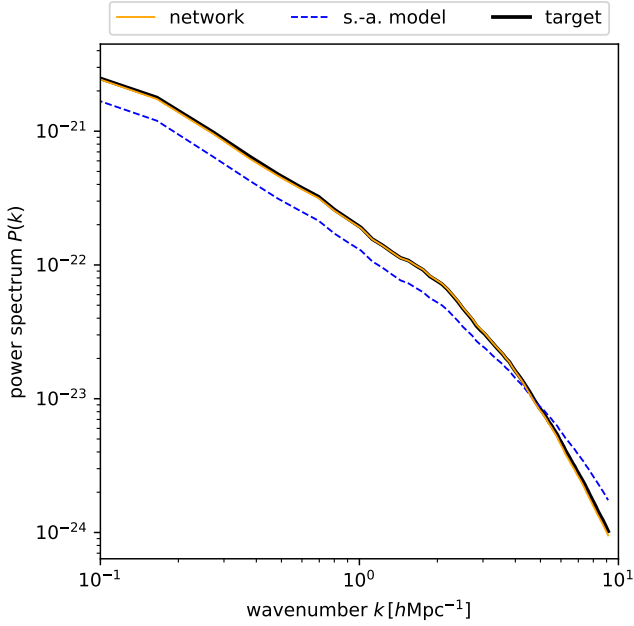


Figure 11. Electron density power spectrum. The network achieves excellent agreement with the target simulation, which is an indication that electron density is an easier target than both pressure and momentum density.

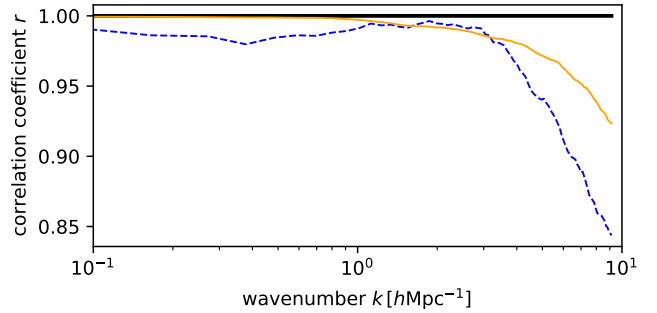


Figure 12. Electron density cross-correlation coefficient with the target simulation.

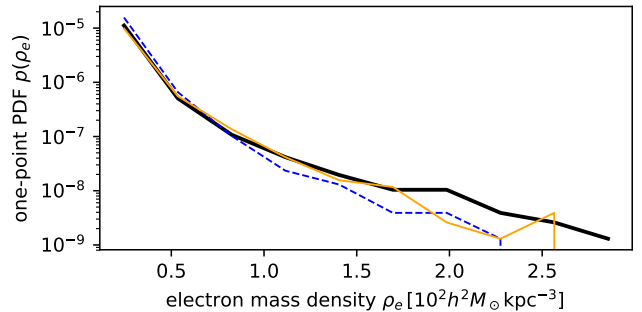


Figure 13. Electron density one-point PDF. Note that the test box is only 10% the size used in Fig. 8, which explains the larger scatter in the tail.

and training procedure was necessary, indicates that the techniques to confront the sparsity problem, explained in Section 4, generalize well to different datasets¹³.

5.3. Electron momentum density

As in the case of the electron density, we find that we do not require the additional zoom-in simulations to learn the mapping to the momentum density; thus, the training set is identical to the one used in the previous section (the sample selection function is slightly different though, c.f. Section 4.1).

The electron momentum density is somewhat special in that \mathbf{p}_e is a three-component vector (while P_e and ρ_e are positive scalars). As mentioned in Section 3.1, one input channel is the dark matter density, and we include information on the dark matter momentum density in the input as well. Then we are left with three possible input-output configurations:

1. three directions as input, three directions as output;
2. three directions as input, one direction as output;
3. one direction as input, one direction as output.

¹³ This is not obvious, since many hyperparameters were tuned during extensive trials on the electron pressure, while the only tuning necessary for the electron density was the biasing of the sample selection function, Eq. 9.

The shape of the semi-analytical model would be chosen equal to the desired output shape. Empirically, we find options 1 and 2 not to work well with network architectures analogous to the one described in Section 3.3. Presumably, the network finds it difficult to learn that it has to establish three separate paths, with small coupling between them. This problem could possibly be solved by modifying the network architecture more fundamentally, however, in the interest of consistency, we choose not to do this and opt for the input-output configuration 3. This necessitates only minor modifications to the network architecture, as described in the caption to Fig. 2. It should be pointed out that this choice has some drawbacks: First, it is probably inefficient, since many features can be assumed to be shared between the three different spatial directions. Second, we could imagine situations in which the dark matter velocity in a particular voxel satisfies inequalities like $v_{\text{DM}}^1 \ll v_{\text{DM}}^2$ (with the superscripts representing different cartesian coordinate directions) and we would like to predict p_e^2 . In such a situation the network would be unable to incorporate small rotations relating the dark matter and electron velocity directions (which would make v_e^2 drastically different from v_{DM}^2), leading to inaccurate predictions of p_e^2 .

Besides the described modifications to the network architecture, we use the tuned sample selection function of Eq. (10), and find that increasing the noise to 20% (c.f. Section 3.4) yields better performance. We observe slight overfitting and halt training after 188 epochs.

In Fig. 14, we plot electron momentum density power spectra. The three plots in the top row represent the three directions, while the larger plot in the bottom row is simply the average of these. Of course, taking this average is not a particularly meaningful operation, given that the momentum components are correlated, but it should serve as a less noisy representation of the network performance. We see that although the network outperforms the simple semi-analytical model, it shows a power deficit of up to 20% in the intermediate k -range. Interestingly, we actually observed a slight power excess when evaluating the network on the validation set, indicating that we overfit on the validation set. As a useful proxy for the actual kSZ-observable, we plot the projected power spectra in Fig. 16 (projections are along the individual momentum directions, which is the physically relevant case). We observe a large variability in the power spectra for the three different directions (top row), making the averaged version less meaningful. It can be seen that the power deficit observed in the 3D power spectra is still present in the projected versions, although upon averaging it is less prominent.

The correlation coefficient shown in Fig. 15 is an average over the three directions, we did not observe significant variability between the directions. We recover correlations exceeding 96% up to $k < 2 h\text{Mpc}^{-1}$, indicating that the predicted momentum field has somewhat lower fidelity than in the cases of electron pressure and density. However, we are comparing correlations at an excellent level here.

It should be noted that the semi-analytical model performs significantly worse than in the other two cases (compare Figs. 7, 12). Since the network builds on the semi-analytical model, worse performance should be expected. From the one-point PDF in Fig. 17 we see that network and semi-analytical model perform about equally well on this summary statistics. One conclusion to be drawn from this is that the deficit in power exhibited by the semi-analytical model cannot be solved by simply rescaling it.

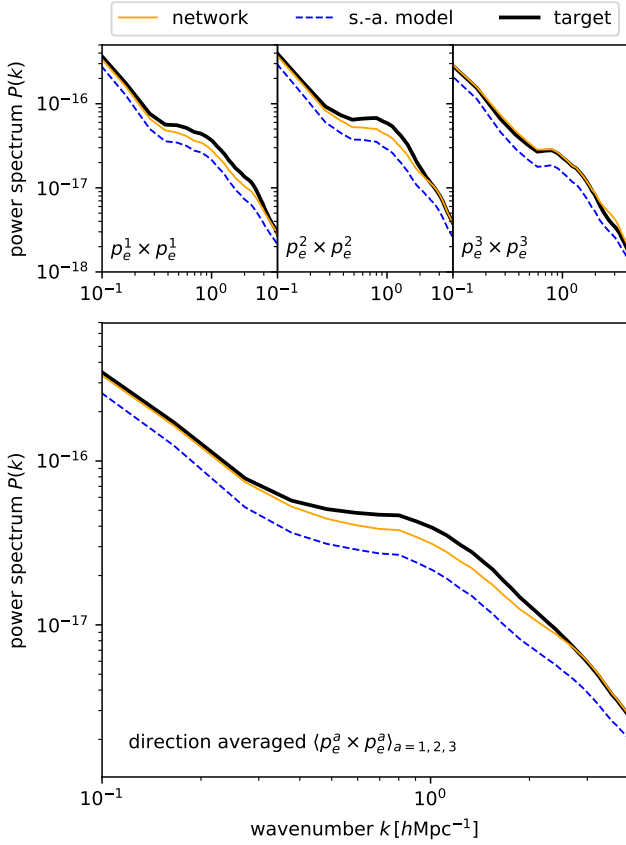


Figure 14. Electron momentum density power spectrum. While the upper panels show the power spectra of the momentum components in three cartesian directions, the lower panel is the average. Although the network performs much better than the semi-analytical model, some discrepancies ($\sim 20\%$) are clearly visible. They are likely related to a combination of overfitting and a sub-optimal network architecture.

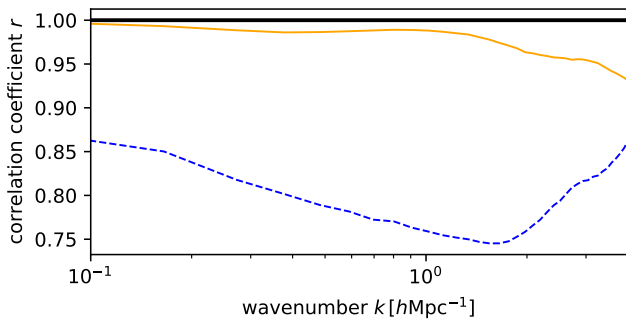


Figure 15. Electron momentum density cross-correlation coefficient with the target simulation, averaged over the three cartesian directions. The scatter between different directions is small.

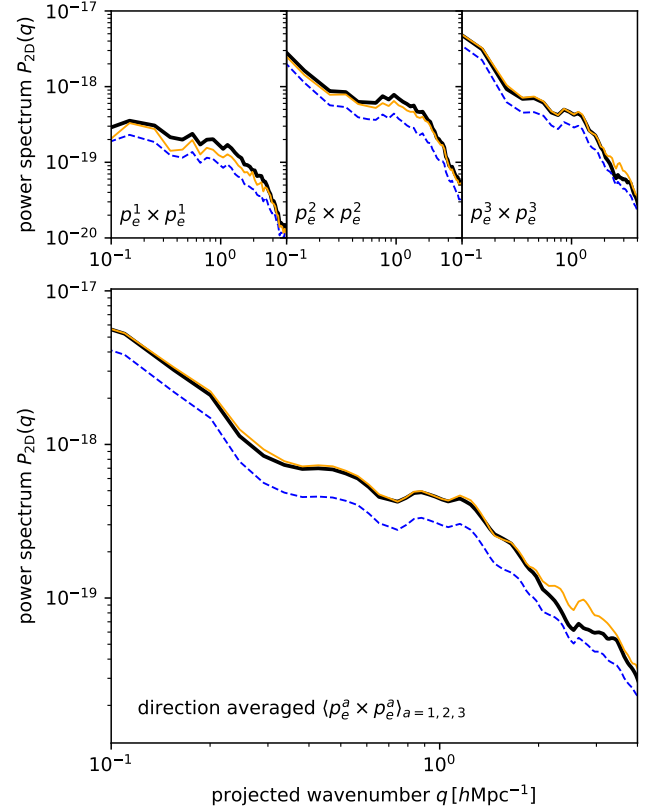


Figure 16. Electron momentum density projected power spectrum. The format is the same as in Fig. 14.

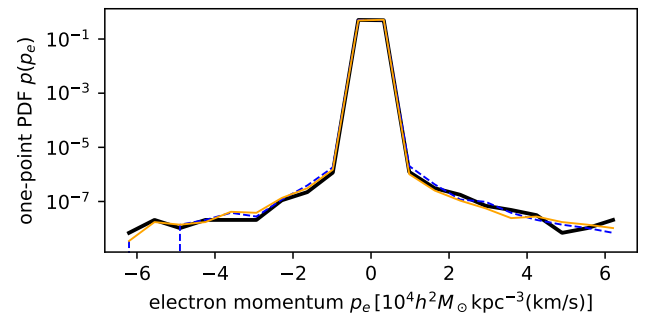


Figure 17. Electron momentum density one-point PDF. Again, all three cartesian directions are included.

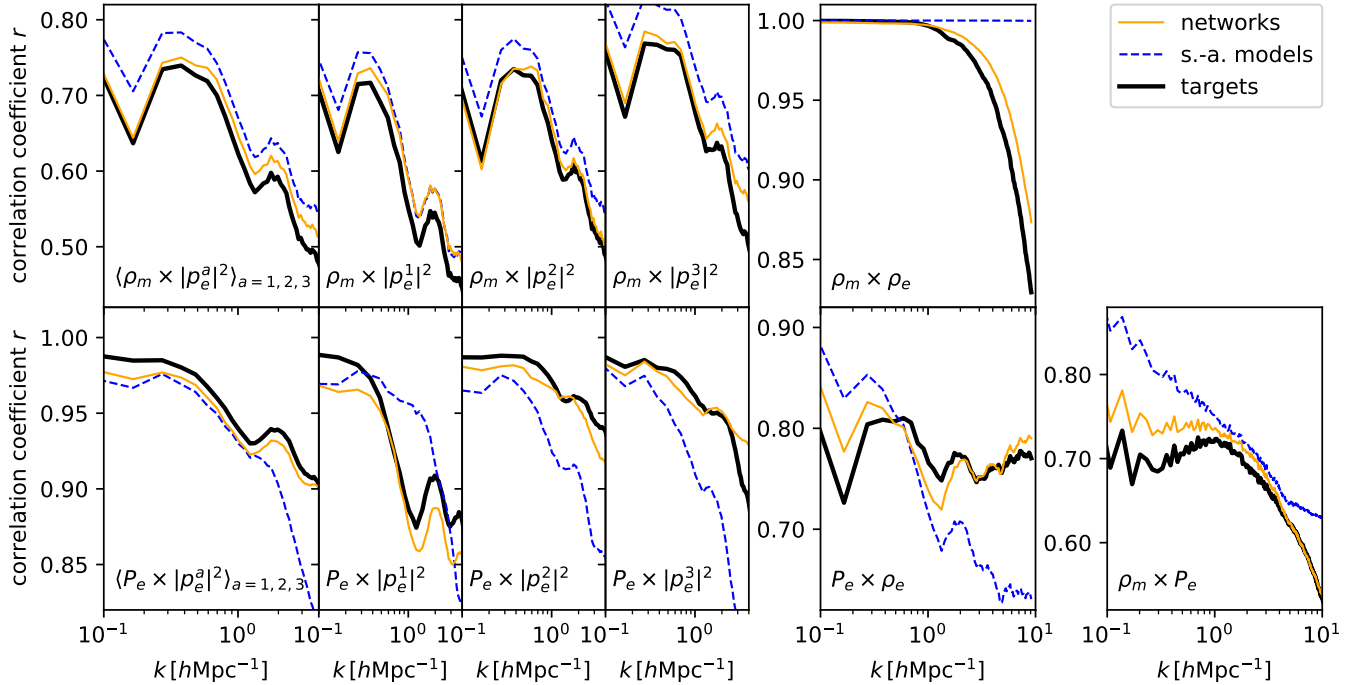


Figure 18. Cross-correlation coefficients between different fields. We observe relatively good agreement between network prediction and target simulation for a range of observables and scales, but discrepancies for others. The networks consistently outperform the semi-analytical models, but it is likely that the network prediction quality depends significantly on the semi-analytical model’s quality.

5.4. Cross-correlations between different fields

As the last part of the section on results, we present cross-correlations between different fields evaluated on the testing set. The purpose of this is twofold. First, correlating different cosmological observables can be less susceptible to systematic effects, which makes them useful summary statistics (e.g., for weak lensing cross tSZ, Hill & Spergel 2014; Van Waerbeke et al. 2014; Hojjati et al. 2017). Second, these cross-correlation functions were not considered during training, making them a “double blind” way of evaluating the network performance (unseen data and new types of summary statistics) and therefore they represent a useful diagnostic.

Fig. 18 shows the 3-dimensional cross-correlations. Note that the ρ_m -field is the same for all correlations including it, since it comes from the gravity-only simulation.

- $\rho_m \times |\mathbf{p}_e|^2$ (element-wise squared): The top left panel in Fig. 18 is direction averaged (with the caveats discussed in Section 5.3), while the narrower panels to its right are for the individual momentum directions. This type of correlation function can be seen as a proxy for weak lensing \times kSZ². The network vastly outperforms the semi-analytical model on larger scales ($k \lesssim 0.5 \text{ hMpc}^{-1}$), while on smaller scales its performance is about a factor two better.
- $P_e \times |\mathbf{p}_e|^2$ (element-wise squared): The panels are arranged analogously to the previous case. This correlation function emulates tSZ \times kSZ² correlations. We observe that the semi-analytical models struggle to generate remotely correct predictions for this correlation function (although the average, perhaps by chance, happens to look reasonable for $k \lesssim 1 \text{ hMpc}^{-1}$). The networks

have problems with this correlation as well, presumably because it combines two predicted fields (while ρ_m in the previous case was correct by design).

- $\rho_m \times \rho_e$: This correlation is mostly a diagnostic and not related to any real-world observable. As expected from the design of the semi-analytical model, Eq. (7), the semi-analytical model’s prediction for ρ_e is perfectly correlated with the matter field. The network’s prediction is closer to the target correlation function.
- $P_e \times \rho_e$: Again, this plot is a diagnostic. As observed before, correlating two generated fields proves to be a challenge for the semi-analytical models. The networks’ prediction is about a factor two better than the semi-analytical models’ for $k \lesssim 1.5 h\text{Mpc}^{-1}$ and much better on smaller scales. We observe the trend already remarked in Section 5.1 that the network prediction for P_e is less accurate on large scales. However, unlike the $P_e \times P_e$ auto-power, projecting the field does not seem to substantially improve the agreement between network prediction and simulation target.
- $\rho_m \times P_e$: This correlation is a proxy for weak lensing \times tSZ statistics. Again, the network struggles on large scales with a correlation function involving P_e , while the small-scale predictions are excellent.

We said at the beginning of this section that considering the cross-correlations has two purposes. With respect to real-world data analyses, we observe high-fidelity predictions for a subset of the correlations and not necessarily in the whole range of wavenumbers considered. However, we point to the fact that, as observed before, projecting the fields can help to bring the networks’ predictions closer to the truth.

With respect to the diagnostic purpose of these plots, we first note that the discrepancies observed here are roughly in line with those seen in different Gaussian summary statistics before, indicating that we did not strongly overfit on the type of summary statistics. A final comment is that we find the discrepancies between network predictions and truth to be mostly in the direction of the discrepancies between semi-analytical models and truth. This is an indication that the network performance depends substantially on the semi-analytical model’s quality.

6. CONCLUSIONS

As part of an effort to quickly generate maps of non-linear observables, we have developed machine learning techniques that allow us to map the gravity-only matter field to three electron gas properties, namely pressure, density, and momentum density. This is the first step towards the generation of Sunyaev-Zel’dovich maps solely from gravity-only simulations, or even from high-redshift initial conditions.

In this work, we have focused on the three-dimensional fields at redshift $z = 0$. We have trained a deep convolutional neural network with a U-Net architecture using the output of cosmological gravity-only and full-physics hydrodynamical simulations from the IllustrisTNG project, specifically the TNG300 box and TNG-Cluster, a set of zoom-in cluster simulations. We have shown that the network outputs match the reference target simulation better than the predictions from simple semi-analytical models, according to a range of summary statistics. To achieve this, we have encountered the problem of sparse data sets, and explained a number of techniques that enabled us to solve it.

While we cannot, at present, exactly quantify the speed-up gained by our technique, it is clear that it will enable us to generate much larger sky areas than would be possible with computationally expensive hydrodynamical simulations. As point of reference, running the reference simulation used in this work, TNG300, took 34.9M CPU-hours, while evaluating the neural network on the same volume took 16 GPU-hours. In order to construct a light-cone, we would probably require evaluation on a few dozen redshift slices.

Some interesting findings made in the course of this work, and explained in more detail in previous sections, are: (1) the networks do not assign much weight to voxel-scale features; (2) the mapping between dark matter and electron pressure is dominated by sub-halo-scale features; (3) electron density is a much easier target than pressure, indicating that the degree of sparsity influences the network prediction quality.

Sub-optimal network performance in some cases (kSZ, some cross-correlations) can be explained by three factors: (1) scarcity of training data (leading to overfitting in some cases); (2) sub-optimal network architecture for the kSZ effect; (3) sub-optimal quality of the semi-analytical models. We believe that these problems are technical in nature and do not present a fundamental obstacle. For example, one could re-calibrate the B12 semi-analytical model for different simulations.

This work is only the first step in a longer program. While we only work at redshift $z = 0$, this is the prerequisite for the prediction of light cones. A further obvious and easy generalization would be to the relativistic tSZ effect (Nozawa et al. 2006; Remazeilles & Chluba 2020; Lee et al. 2020). Another extension would be to X-ray maps, for which excellent observational data will be available from ROSAT and eROSITA. Due to the signal’s dependence on the square of the electron density the sparsity problem is likely quite severe; the data augmentation with zoom-in simulations which we used for the tSZ effect will be essential in that case.

In terms of future work, a clear goal is the generalization to redshifts $z \neq 0$, which will ultimately enable us to generate maps of actual observables. There is a good chance that the dependence on redshift is a relatively simple function; this would imply that we would effectively enlarge the training data set and mitigate the overfitting problem. While we have worked with a single simulation (TNG300) so far, there is a need to compare networks trained on different simulations (one could also imagine mixing samples with different sub-grid physics, although the outcome of such a training strategy should be validated thoroughly). A possible route could be to use the CAMEL simulations (Villaescusa-Navarro et al. in prep.), which contain state-of-the-art hydrodynamical simulations spanning thousands of different cosmologies and astrophysics models run with two different hydrodynamical solvers and subgrid implementations.

As mentioned in the Introduction, our approach does not capture stochasticity in the mapping from gravity-only matter to electron gas. The probabilistic nature stems from unresolved features that are coupled to the scales of interest, for example, from the stochasticity in the efficiency of AGN feedback. Possible extensions to this work which would take this effect into account could involve GANs (Goodfellow et al. 2014) or Bayesian neural networks (Tishby et al. 1989). We note that with GANs it would be challenging to generate large enough volumes such that the two-halo term is captured correctly. A further difficulty in both approaches would be to create consistent predictions of several different observables, as is required for the cross-correlation functions. However, we believe that stochasticity does not present a fundamental obstacle to our approach, since it could accurately be modeled as additional white noise in any parameter inference.

Our work opens up the avenue towards several possible applications. Given the ability to quickly generate maps of the Sunyaev-Zel'dovich effects and other observables, we could create covariance matrices and perform parameter inference from summary statistics. In order to utilize the non-Gaussian information in maps, likelihood-free inference (Alsing et al. 2018) could be a promising approach; for example applied to the tSZ one-point PDF (Hill et al. 2014; Thiele et al. 2019). Furthermore, we could imagine interpreting the network output to learn more about the effect of sub-grid astrophysical models.

ACKNOWLEDGMENTS

We would like to thank J.C. Hill and E. Komatsu for useful suggestions. The training of the neural networks has been carried out on the Tiger supercomputer of Princeton University. We thank their system administrators for their help at several stages of this work. FVN acknowledges funding from the WFIRST program through NNG26PJ30C and NNN12AA01C. The Flatiron Institute is supported by the Simons Foundation. The IllustrisTNG simulations including TNG300 were undertaken with compute time awarded by the Gauss Centre for Supercomputing (GCS) under GCS Large-Scale Projects GCS-ILLU and GCS-DWAR on the Hazel Hen supercomputer at the High Performance Computing Center Stuttgart (HLRS). The TNG-Cluster simulation has been executed on Draco and Cobra machines of the Max Planck Computing and Data Facility (MPCDF) in Garching, Germany.

REFERENCES

- Afshordi, N., Lin, Y.-T., Nagai, D., & Sanderson, A. J. R. 2007, *MNRAS*, 378, 293, doi: [10.1111/j.1365-2966.2007.11776.x](https://doi.org/10.1111/j.1365-2966.2007.11776.x)
- Agarwal, S., Davé, R., & Bassett, B. A. 2018, *MNRAS*, 478, 3410, doi: [10.1093/mnras/sty1169](https://doi.org/10.1093/mnras/sty1169)
- Allison, J. R., Taylor, A. C., Jones, M. E., Rawlings, S., & Kay, S. T. 2011, *MNRAS*, 410, 341, doi: [10.1111/j.1365-2966.2010.17447.x](https://doi.org/10.1111/j.1365-2966.2010.17447.x)
- Alsing, J., Wandelt, B., & Feeney, S. 2018, *MNRAS*, 477, 2874, doi: [10.1093/mnras/sty819](https://doi.org/10.1093/mnras/sty819)
- Alvarez, M. A. 2016, *ApJ*, 824, 118, doi: [10.3847/0004-637X/824/2/118](https://doi.org/10.3847/0004-637X/824/2/118)
- Arnaud, M., Pratt, G. W., Piffaretti, R., et al. 2010, *A&A*, 517, A92, doi: [10.1051/0004-6361/200913416](https://doi.org/10.1051/0004-6361/200913416)
- Atrio-Barandela, F., Kashlinsky, A., Kocevski, D., & Ebeling, H. 2008, *ApJL*, 675, L57, doi: [10.1086/533437](https://doi.org/10.1086/533437)
- Battaglia, N. 2016, *JCAP*, 2016, 058, doi: [10.1088/1475-7516/2016/08/058](https://doi.org/10.1088/1475-7516/2016/08/058)
- Battaglia, N., Bond, J. R., Pfrommer, C., & Sievers, J. L. 2012, *ApJ*, 758, 75, doi: [10.1088/0004-637X/758/2/75](https://doi.org/10.1088/0004-637X/758/2/75)
- Battaglia, N., Bond, J. R., Pfrommer, C., Sievers, J. L., & Sijacki, D. 2010, *ApJ*, 725, 91, doi: [10.1088/0004-637X/725/1/91](https://doi.org/10.1088/0004-637X/725/1/91)
- Bode, P., Ostriker, J. P., & Vikhlinin, A. 2009, *ApJ*, 700, 989, doi: [10.1088/0004-637X/700/2/989](https://doi.org/10.1088/0004-637X/700/2/989)
- Bode, P., Ostriker, J. P., Weller, J., & Shaw, L. 2007, *ApJ*, 663, 139, doi: [10.1086/518432](https://doi.org/10.1086/518432)
- Capelo, P. R., Coppi, P. S., & Natarajan, P. 2012, *MNRAS*, 422, 686, doi: [10.1111/j.1365-2966.2012.20648.x](https://doi.org/10.1111/j.1365-2966.2012.20648.x)
- Chaudhuri, A., & Majumdar, S. 2011, *ApJL*, 728, L41, doi: [10.1088/2041-8205/728/2/L41](https://doi.org/10.1088/2041-8205/728/2/L41)
- da Silva, A. C., Barbosa, D., Liddle, A. R., & Thomas, P. A. 2000, *MNRAS*, 317, 37, doi: [10.1046/j.1365-8711.2000.03553.x](https://doi.org/10.1046/j.1365-8711.2000.03553.x)
- . 2001, *MNRAS*, 326, 155, doi: [10.1046/j.1365-8711.2001.04580.x](https://doi.org/10.1046/j.1365-8711.2001.04580.x)
- Dolag, K., Komatsu, E., & Sunyaev, R. 2016, *MNRAS*, 463, 1797, doi: [10.1093/mnras/stw2035](https://doi.org/10.1093/mnras/stw2035)
- Duffy, A. R., Schaye, J., Kay, S. T., & Dalla Vecchia, C. 2008, *MNRAS*, 390, L64, doi: [10.1111/j.1745-3933.2008.00537.x](https://doi.org/10.1111/j.1745-3933.2008.00537.x)

- Efstathiou, G., & Migliaccio, M. 2012, *MNRAS*, 423, 2492, doi: [10.1111/j.1365-2966.2012.21059.x](https://doi.org/10.1111/j.1365-2966.2012.21059.x)
- Goodfellow, I. J., Pouget-Abadie, J., Mirza, M., et al. 2014, arXiv e-prints, arXiv:1406.2661. <https://arxiv.org/abs/1406.2661>
- Gupta, N., Saro, A., Mohr, J. J., Dolag, K., & Liu, J. 2017, *MNRAS*, 469, 3069, doi: [10.1093/mnras/stx715](https://doi.org/10.1093/mnras/stx715)
- Hallman, E. J., Burns, J. O., Motl, P. M., & Norman, M. L. 2007a, *ApJ*, 665, 911, doi: [10.1086/519447](https://doi.org/10.1086/519447)
- Hallman, E. J., O’Shea, B. W., Norman, M. L., Wagner, R., & Burns, J. O. 2007b, in *Heating versus Cooling in Galaxies and Clusters of Galaxies*, ed. H. Böhringer, G. W. Pratt, A. Finoguenov, & P. Schuecker, 355, doi: [10.1007/978-3-540-73484-0_64](https://doi.org/10.1007/978-3-540-73484-0_64)
- Hand, N., Feng, Y., Beutler, F., et al. 2018, *AJ*, 156, 160, doi: [10.3847/1538-3881/aadae0](https://doi.org/10.3847/1538-3881/aadae0)
- He, S., Li, Y., Feng, Y., et al. 2019, *Proceedings of the National Academy of Science*, 116, 13825, doi: [10.1073/pnas.1821458116](https://doi.org/10.1073/pnas.1821458116)
- Hill, J. C., & Spergel, D. N. 2014, *JCAP*, 2014, 030, doi: [10.1088/1475-7516/2014/02/030](https://doi.org/10.1088/1475-7516/2014/02/030)
- Hill, J. C., Sherwin, B. D., Smith, K. M., et al. 2014, arXiv e-prints, arXiv:1411.8004. <https://arxiv.org/abs/1411.8004>
- Hojjati, A., Tröster, T., Harnois-Déraps, J., et al. 2017, *MNRAS*, 471, 1565, doi: [10.1093/mnras/stx1659](https://doi.org/10.1093/mnras/stx1659)
- Jaffe, A. H., & Kamionkowski, M. 1998, *PhRvD*, 58, 043001, doi: [10.1103/PhysRevD.58.043001](https://doi.org/10.1103/PhysRevD.58.043001)
- Jo, Y., & Kim, J.-h. 2019, *MNRAS*, 489, 3565, doi: [10.1093/mnras/stz2304](https://doi.org/10.1093/mnras/stz2304)
- Kay, S. T., Peel, M. W., Short, C. J., et al. 2012, *MNRAS*, 422, 1999, doi: [10.1111/j.1365-2966.2012.20623.x](https://doi.org/10.1111/j.1365-2966.2012.20623.x)
- Komatsu, E., & Kitayama, T. 1999, *ApJL*, 526, L1, doi: [10.1086/312364](https://doi.org/10.1086/312364)
- Komatsu, E., & Seljak, U. 2001, *MNRAS*, 327, 1353, doi: [10.1046/j.1365-8711.2001.04838.x](https://doi.org/10.1046/j.1365-8711.2001.04838.x)
- . 2002, *MNRAS*, 336, 1256, doi: [10.1046/j.1365-8711.2002.05889.x](https://doi.org/10.1046/j.1365-8711.2002.05889.x)
- Le Brun, A. M. C., McCarthy, I. G., Schaye, J., & Ponman, T. J. 2014, *MNRAS*, 441, 1270, doi: [10.1093/mnras/stu608](https://doi.org/10.1093/mnras/stu608)
- . 2017, *MNRAS*, 466, 4442, doi: [10.1093/mnras/stw3361](https://doi.org/10.1093/mnras/stw3361)
- Lee, E., Chluba, J., Kay, S. T., & Barnes, D. J. 2020, *MNRAS*, 493, 3274, doi: [10.1093/mnras/staa450](https://doi.org/10.1093/mnras/staa450)
- Lee, J., & Suto, Y. 2003, *ApJ*, 585, 151, doi: [10.1086/345931](https://doi.org/10.1086/345931)
- Ma, C.-P., & Fry, J. N. 2002, *PhRvL*, 88, 211301, doi: [10.1103/PhysRevLett.88.211301](https://doi.org/10.1103/PhysRevLett.88.211301)
- Marinacci, F., Vogelsberger, M., Pakmor, R., et al. 2018, *MNRAS*, 480, 5113, doi: [10.1093/mnras/sty2206](https://doi.org/10.1093/mnras/sty2206)
- Mead, A. J., Tröster, T., Heymans, C., Van Waerbeke, L., & McCarthy, I. G. 2020, arXiv e-prints, arXiv:2005.00009. <https://arxiv.org/abs/2005.00009>
- Moster, B. P., Naab, T., Lindström, M., & O’Leary, J. A. 2020, arXiv e-prints, arXiv:2005.12276. <https://arxiv.org/abs/2005.12276>
- Nagai, D., Kravtsov, A. V., & Vikhlinin, A. 2007, *ApJ*, 668, 1, doi: [10.1086/521328](https://doi.org/10.1086/521328)
- Naiman, J. P., Pillepich, A., Springel, V., et al. 2018, *MNRAS*, 477, 1206, doi: [10.1093/mnras/sty618](https://doi.org/10.1093/mnras/sty618)
- Navarro, J. F., Frenk, C. S., & White, S. D. M. 1997, *ApJ*, 490, 493, doi: [10.1086/304888](https://doi.org/10.1086/304888)
- Nelson, D., Pillepich, A., Springel, V., et al. 2018, *MNRAS*, 475, 624, doi: [10.1093/mnras/stx3040](https://doi.org/10.1093/mnras/stx3040)
- Nelson, D., Springel, V., Pillepich, A., et al. 2019, *Computational Astrophysics and Cosmology*, 6, 2, doi: [10.1186/s40668-019-0028-x](https://doi.org/10.1186/s40668-019-0028-x)
- Nelson, K., Lau, E. T., & Nagai, D. 2014, *ApJ*, 792, 25, doi: [10.1088/0004-637X/792/1/25](https://doi.org/10.1088/0004-637X/792/1/25)
- Nelson et al. in prep.
- Nozawa, S., Itoh, N., Suda, Y., & Ohhata, Y. 2006, *Nuovo Cimento B Serie*, 121, 487, doi: [10.1393/ncb/i2005-10223-0](https://doi.org/10.1393/ncb/i2005-10223-0)
- Ostriker, J. P., Bode, P., & Babul, A. 2005, *ApJ*, 634, 964, doi: [10.1086/497122](https://doi.org/10.1086/497122)
- Ostriker, J. P., & Vishniac, E. T. 1986, *ApJL*, 306, L51, doi: [10.1086/184704](https://doi.org/10.1086/184704)
- Park, H., Alvarez, M. A., & Bond, J. R. 2018, *ApJ*, 853, 121, doi: [10.3847/1538-4357/aaa0da](https://doi.org/10.3847/1538-4357/aaa0da)
- Park, H., Komatsu, E., Shapiro, P. R., Koda, J., & Mao, Y. 2016, *ApJ*, 818, 37, doi: [10.3847/0004-637X/818/1/37](https://doi.org/10.3847/0004-637X/818/1/37)
- Persi, F. M., Spergel, D. N., Cen, R., & Ostriker, J. P. 1995, *ApJ*, 442, 1, doi: [10.1086/175416](https://doi.org/10.1086/175416)
- Pfrommer, C., Enßlin, T. A., Springel, V., Jubelgas, M., & Dolag, K. 2007, *MNRAS*, 378, 385, doi: [10.1111/j.1365-2966.2007.11732.x](https://doi.org/10.1111/j.1365-2966.2007.11732.x)

- Pillepich, A., Nelson, D., Hernquist, L., et al. 2018a, MNRAS, 475, 648, doi: [10.1093/mnras/stx3112](https://doi.org/10.1093/mnras/stx3112)
- Pillepich, A., Springel, V., Nelson, D., et al. 2018b, MNRAS, 473, 4077, doi: [10.1093/mnras/stx2656](https://doi.org/10.1093/mnras/stx2656)
- Planck Collaboration, Ade, P. A. R., Aghanim, N., et al. 2013, A&A, 550, A131, doi: [10.1051/0004-6361/201220040](https://doi.org/10.1051/0004-6361/201220040)
- Planelles, S., Fabjan, D., Borgani, S., et al. 2017, MNRAS, 467, 3827, doi: [10.1093/mnras/stx318](https://doi.org/10.1093/mnras/stx318)
- Ramos-Ceja, M. E., Basu, K., Pacaud, F., & Bertoldi, F. 2015, A&A, 583, A111, doi: [10.1051/0004-6361/201425534](https://doi.org/10.1051/0004-6361/201425534)
- Refregier, A., Komatsu, E., Spergel, D. N., & Pen, U.-L. 2000, PhRvD, 61, 123001, doi: [10.1103/PhysRevD.61.123001](https://doi.org/10.1103/PhysRevD.61.123001)
- Remazeilles, M., & Chluba, J. 2020, MNRAS, 494, 5734, doi: [10.1093/mnras/staa1135](https://doi.org/10.1093/mnras/staa1135)
- Scaramella, R., Cen, R., & Ostriker, J. P. 1993, ApJ, 416, 399, doi: [10.1086/173245](https://doi.org/10.1086/173245)
- Schäfer, B. M., Pfrommer, C., Bartelmann, M., Springel, V., & Hernquist, L. 2006, MNRAS, 370, 1309, doi: [10.1111/j.1365-2966.2006.10552.x](https://doi.org/10.1111/j.1365-2966.2006.10552.x)
- Schaye, J., Crain, R. A., Bower, R. G., et al. 2015, MNRAS, 446, 521, doi: [10.1093/mnras/stu2058](https://doi.org/10.1093/mnras/stu2058)
- Shaw, L. D., Nagai, D., Bhattacharya, S., & Lau, E. T. 2010, ApJ, 725, 1452, doi: [10.1088/0004-637X/725/2/1452](https://doi.org/10.1088/0004-637X/725/2/1452)
- Shaw, L. D., Rudd, D. H., & Nagai, D. 2012, ApJ, 756, 15, doi: [10.1088/0004-637X/756/1/15](https://doi.org/10.1088/0004-637X/756/1/15)
- Shi, X., & Komatsu, E. 2014, MNRAS, 442, 521, doi: [10.1093/mnras/stu858](https://doi.org/10.1093/mnras/stu858)
- Sijacki, D., Pfrommer, C., Springel, V., & Enßlin, T. A. 2008, MNRAS, 387, 1403, doi: [10.1111/j.1365-2966.2008.13310.x](https://doi.org/10.1111/j.1365-2966.2008.13310.x)
- Spacek, A., Richardson, M. L. A., Scannapieco, E., et al. 2018, ApJ, 865, 109, doi: [10.3847/1538-4357/aada01](https://doi.org/10.3847/1538-4357/aada01)
- Springel, V., White, M., & Hernquist, L. 2001, ApJ, 549, 681, doi: [10.1086/319473](https://doi.org/10.1086/319473)
- Springel, V., Pakmor, R., Pillepich, A., et al. 2018, MNRAS, 475, 676, doi: [10.1093/mnras/stx3304](https://doi.org/10.1093/mnras/stx3304)
- Strobl, S., Formella, A., & Pöschel, T. 2016, Journal of Computational Physics, 311, 158, doi: <https://doi.org/10.1016/j.jcp.2016.02.003>
- Sunyaev, R. A., & Zeldovich, Y. B. 1970, Ap&SS, 7, 3, doi: [10.1007/BF00653471](https://doi.org/10.1007/BF00653471)
- Thiele, L., Hill, J. C., & Smith, K. M. 2019, PhRvD, 99, 103511, doi: [10.1103/PhysRevD.99.103511](https://doi.org/10.1103/PhysRevD.99.103511)
- Tishby, N., Levin, E., & Solla, S. 1989, in IJCNN Int Jt Conf Neural Network, ed. Anon (Publ by IEEE), 403–409
- Trac, H., Bode, P., & Ostriker, J. P. 2011, ApJ, 727, 94, doi: [10.1088/0004-637X/727/2/94](https://doi.org/10.1088/0004-637X/727/2/94)
- Tröster, T., Ferguson, C., Harnois-Déraps, J., & McCarthy, I. G. 2019, MNRAS, 487, L24, doi: [10.1093/mnrasl/slz075](https://doi.org/10.1093/mnrasl/slz075)
- Valageas, P., Balbi, A., & Silk, J. 2001, A&A, 367, 1, doi: [10.1051/0004-6361:20000403](https://doi.org/10.1051/0004-6361:20000403)
- Van Waerbeke, L., Hinshaw, G., & Murray, N. 2014, PhRvD, 89, 023508, doi: [10.1103/PhysRevD.89.023508](https://doi.org/10.1103/PhysRevD.89.023508)
- Villaescusa-Navarro, F. 2018, Pylans: Python libraries for the analysis of numerical simulations. <http://ascl.net/1811.008>
- Villaescusa-Navarro et al. in prep.
- Vishniac, E. T. 1987, ApJ, 322, 597, doi: [10.1086/165755](https://doi.org/10.1086/165755)
- Weinberger, R., Springel, V., Hernquist, L., et al. 2017, MNRAS, 465, 3291, doi: [10.1093/mnras/stw2944](https://doi.org/10.1093/mnras/stw2944)
- White, M., Hernquist, L., & Springel, V. 2002, ApJ, 579, 16, doi: [10.1086/342756](https://doi.org/10.1086/342756)
- Xu, X., Ho, S., Trac, H., et al. 2013, ApJ, 772, 147, doi: [10.1088/0004-637X/772/2/147](https://doi.org/10.1088/0004-637X/772/2/147)
- Zandanel, F., Pfrommer, C., & Prada, F. 2014, MNRAS, 438, 116, doi: [10.1093/mnras/stt2196](https://doi.org/10.1093/mnras/stt2196)
- Zeldovich, Y. B., & Sunyaev, R. A. 1969, Ap&SS, 4, 301, doi: [10.1007/BF00661821](https://doi.org/10.1007/BF00661821)
- Zhang, P., Pen, U.-L., & Trac, H. 2004, MNRAS, 347, 1224, doi: [10.1111/j.1365-2966.2004.07298.x](https://doi.org/10.1111/j.1365-2966.2004.07298.x)
- Zhang, X., Wang, Y., Zhang, W., et al. 2019, arXiv e-prints, arXiv:1902.05965. <https://arxiv.org/abs/1902.05965>

APPENDIX

A. PIXELIZATION

Our primary input data are properties of the dark matter field from the gravity-only simulations. For prediction of the electron pressure and density, we use the dark matter density, while for the electron momentum density we also use the dark matter momentum density. We make use of the `subfind_hsm1` fields in the snapshot to obtain spheres of varying size in which we assume the dark matter properties to be uniform; then we use the `Overlap` library¹⁴ (Strobl et al. 2016) to grid these spheres onto cubical voxels. The target data (electron pressure, density, and momentum density) are taken from the hydrodynamical run. Here, we approximate the Voronoi cells as spheres, the radius being inferred from the volume given in the simulation snapshot, and perform the gridding to voxels as described. These gridding procedures are approximations whose accuracy improves as the number of simulation elements in the individual voxels increases. Thus, these approximations are not worrisome in the high-density regions we are primarily focused on in this work. We note that the electron pressure is not directly measured in the simulation; however, under the assumption of complete ionization a linear relationship between thermal and electron pressure allows us to infer the latter. For reference, $P_{\text{th}}/P_e = (5X_{\text{H}} + 3)/2(X_{\text{H}} + 1) = 1.932$, with X_{H} the primordial hydrogen mass fraction.

B. TRAINING BOXES

As justified in Section 3.2, we restrict the target volumes to cubical boxes of size $(3.2 h^{-1}\text{Mpc})^3$; the semi-analytical models are evaluated on the same volume. The dark matter samples serving as input are taken as boxes of twice the sidelength, i.e. volume $(6.4 h^{-1}\text{Mpc})^3$; the target volume is centred in these boxes. The additional padding of $1.6 h^{-1}\text{Mpc}$ on each side of the target volume allows for inclusion of long-range effects. For electron pressure and density, we use voxels of sidelength $100.1 h^{-1}\text{kpc}$, such that the dark matter (electron gas) boxes are of size 64^3 (32^3) voxels. For the electron momentum density we use half this resolution (voxel sidelength $200.2 h^{-1}\text{kpc}$). We chose the resolution by two considerations: (1) we do not expect structure below length-scales of a few $100 h^{-1}\text{kpc}$ to be important in the mapping from dark matter to electron gas, while observationally smaller scales should also be of minor importance; (2) higher resolutions would be difficult to implement on the hardware available to us, the limiting factor is GPU memory.

For electron density and momentum density as targets, we split the TNG300 box into training (70%), validation (20%), and testing (10%) cuboidal sub-boxes. For the electron pressure we use external data for training (as discussed in Section 4.1), allowing us to use the whole simulation box for testing (we also use 20% of the box for validation, leading to an overlap between validation and testing data; however, the small volume in comparison to the testing box ensures that this does not invalidate the testing results).

C. TRANSFORMATIONS

The numerical values a , b , c introduced in Eq. (11) are as follows:

¹⁴ <https://github.com/severinstrobl/overlap>

	target = P_e	target = ρ_e	target = \mathbf{p}_e	
	$x_{\text{DM}} = \rho_m$	$x_{\text{DM}} = \rho_m$	$x_{\text{DM}} = \rho_m$	$x_{\text{DM}} = \mathbf{p}_m$
<i>a</i>	2.2939	2.2160	8.4592	1.8813
<i>b</i>	2.7984×10^6	2.7984×10^6	3.9381×10^6	1.2871×10^4
<i>c</i>	3.8477×10^{-1}	3.8232×10^{-1}	2.6845×10^{-2}	0.0000

We remind the reader of the unit conventions given in footnote 6. The calculations for *a*, *b*, and *c* were performed by restricting to “interesting” voxels in the sense of Section 4.1, these definitions were slightly different for different targets which explains the different values.